Scaling and classification of a minijet-manipulated turbulent jet

Dewei Fan and Yu Zhou[*]

Center for Turbulence Control, Harbin Institute of Technology, Shenzhen 518055, China

A turbulent round jet is experimentally manipulated using a pulsed periodic radial minijet placed near the nozzle exit. The actuation is characterized by the frequency f_a, duty cycle α, and mass-flow ratio C_m. The flow is measured at a Reynolds number of 8000, based on jet exit velocity and diameter, using the techniques of hot wire, flow visualization. and particle image velocimetry. Following Zhou *et al.* [J. Fluid Mech. **897**, A27 (2020)], the jet decay rate of the centerline mean velocity K is employed as a surrogate for jet mixing. The optimum f_a corresponding to the maximum K is observed to be one-half of the preferred mode frequency f_0 of main jet, i.e., $f_a/f_0 = 0.5$. Measurements indicate that K depends on C_m and α given $f_a/f_0 = 0.5$. It is found that once K, C_m, and α are corrected and replaced by their "true values" K^c, C_m^c, and α^c, $K = g_1(C_m, \alpha)$ may be reduced to $K^c = g_2(\xi^c)$, where g_1 and g_2 are different functions and the scaling factor $\xi^c = C_m^c/\alpha^c$, which represents physically the effective penetration depth of the minijet and, unlike previous report, determines uniquely K^c. The manipulated jet is further classified into five typical flow structures, i.e., monomodal I, deflection I, bifurcation, monomodal II, and deflection II, which are uniquely determined by ξ^c. These representative flow structures are connected to the initial interactions between the minijet and the main jet.

I. INTRODUCTION

Turbulent round jets are of great interest due to their wide existence in industrial applications. The coherent structures in a turbulent jet are characterized by a large range of scales, varying convection velocity, and a rich set of three-dimensional patterns [1]. These structures are highly susceptible to upstream forcing near the nozzle exit [2,3]. The understanding of their underlying mechanisms will guide the successful design of practical engineering applications, such as the mixing enhancement [4,5] and noise reduction [6–8].

Over the past few decades, many passive techniques have been proposed to improve jet mixing. Passive techniques are based on modifying nozzle geometry, such as noncircular nozzles [9–12], chevron nozzles [13,14], and adding Zaman tabs [15,16]. Passive control faces two challenges. First, the shape of the jet nozzle is fixed and cannot adapt to the changes in the flow state. Second, the control performance tends to decrease with increasing Reynolds number. Active control may overcome these problems, albeit at the expense of an energy expenditure [17–19]. Davis [20] proposed a jet-mixing enhancement using two steady-jet actuators at a Mach number of 0.8. This technique increases jet mixing to the level of tabs, although with a fraction of thrust loss. New and Tay [21] attributed the enhanced mixing to a counter-rotating vortex pair produced by the injection of each steady control jet. The actuation distorts the cross-sectional shape and centerline mean velocity decay of main jet. Seidel *et al.* [22] experimentally investigated various radial blowing

---

*[*]yuzhou@hit.edu.cn

configurations and demonstrated that placing steady control jets around the circular jet exit may mimic well noncircular jets, greatly enhancing mixing.

The control performance can be significantly improved when the control jets are made unsteady or periodically pulsing [23]. This is due to two reasons. First, the unsteady injection is associated with a higher maximum velocity [24,25], thus producing a deeper penetration into the main jet and a stronger effect on the coherent structures [26,27]. Second, the periodic excitation perturbations excite the inherent instabilities of the main jet [28]. Yang and Zhou [29] conducted a detailed investigation on the effect of the mass-flow rate and actuation frequency on a turbulent round jet (Re = 8000) using two unsteady minijets. Three types of coherent structures are identified, i.e., contorted ring vortices, two pairs of streamwise vortices, and mushroomlike counter-rotating structures, all acting to enhance mixing.

Flow control based on an unsteady control jet may often involve many control parameters such as the duty cycle (α) of the control jet, the mass-flow ratio C_m, excitation frequency ratio f_a/f_0 (f_0 is the preferred-mode frequency of the main jet), and ratio d/D, where d and D are the exit diameters of the control jet and main jet, respectively. While the deployment of multiple control parameters enlarges the control space and performance, it may make control highly complicated, resulting in a tremendous difficulty in finding the optimum or near-optimal solution, along with gaining the physical understanding of control. As such, it is highly desirable to find a single control parameter or a scaling law which is directly related to the control performance [30,31]. The scaling law is very important for possible engineering applications since the flow structure and the similarity parameters obtained from a laboratory-scale model are the same as those of a full-scale model [32]. In the manipulation of a turbulent jet using a single unsteady minijet, Perumal and Zhou [25] investigated the dependence of the decay rate K of jet centerline mean velocity on α, C_m, f_a/f_0, and d/D. They found a scaling factor ξ so that the relationship $K = g_3 (C_m, f_a/f_0, d/D, \alpha)$ may be reduced to $K = g_4(\xi)$, where g_3 and g_4 are different functions and $\xi = \frac{\sqrt{MR}}{\alpha}(\frac{d}{D})^n$ ($\sqrt{MR} = C_m(D/d)$) is the momentum ratio of the minijet to the main jet and n is a factor, varying with α). However, because of the occurrence of complex physical mechanisms under control, the scaling law is divided into four branches once ξ exceeds its optimal value where K reaches the maximum. One important issue arises. Can we reduce the four branches into a single one based on an in-depth understanding of these physical mechanisms? A simplified scaling law may greatly facilitate practical applications.

Motivated by the above issue, this work will be focused on the manipulation of a turbulent jet using a single unsteady minijet and sets out its goal in threefold. First, categorize the actuation effect in terms of the control parameters. Second, find a simplified scaling law for the relations between the control parameters (C_m, f_a/f_0, d/D, and α) and K. Third, classify the manipulated jet and connect it to how the minijet penetrates into main jet. To this end, extensive measurements are performed using hot wire, flow visualization, and particle image velocimetry (PIV) in the manipulated jet. The paper is organized as follows. The experimental setup is described in Sec. II. The following two sections, Secs. III and IV, present the empirical scaling analysis based on experimental data and the flow structures under control, respectively. The work is summarized in Sec. V.

II. EXPERIMENT DETAILS

A. Experiment setup

Figure 1 shows the schematic of the main jet facility, including an air supply system, a main round jet, and minijet actuator. The main jet is described in detail in Zhou *et al.* [33]. The Reynolds number $Re_D = \overline{U_j}D/\nu$ investigated is 8000, where U_j is the streamwise velocity measured at the nozzle exit, the overbar denotes time averaging, ν is the kinematic viscosity of air, and $D = 20$ mm is the nozzle exit diameter. The center of the jet exit is set as the origin of a right-hand Cartesian coordinate system, where the x axis is aligned with the streamwise direction and the y axis is along the minijet injection direction [Fig. 1(c)].
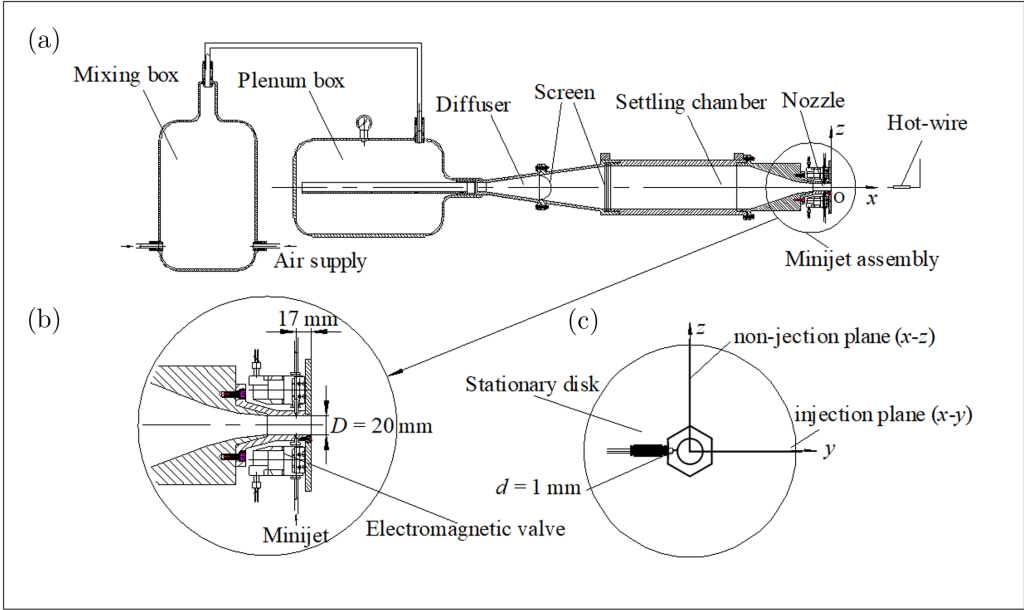
FIG. 1. Sketch of the experimental setup: (a) main jet facility, (b) minijet arrangement, and (c) minijet assembly.

The actuation is performed with a single radial minijet placed at 17mm upstream of the nozzle exit. The minijet mass-flow rate is controlled and measured by a mass-flow controller (FLOWMETHOD FL-802). The actuation strength is characterized by the mass-flow ratio defined by

$$C_m = \dot{m}_{\text{mini}}/\dot{m}_j, \tag{1}$$

where $\dot{m}_{\text{mini}}$ and $\dot{m}_j$ denote the mass-flow rate of minijet and main jet, respectively. The minijet flows through an orifice with a diameter $d = 1$ mm, whose location is shown in Fig. 1(b). The frequency and duty cycle are regulated by an electromagnetic valve (Koganei K2-100SF-09-LL), which is in an on/off mode. The maximum frequency of the valve is 500 Hz, which is more than three times the characteristic shedding frequency of the unforced jet $f_0 = 135$ Hz at $\text{Re}_D = 8000$.

B. Flow measurements

The jet exit velocity was measured at $(x/D, y/D, z/D) = (0, 0, 0)$ with a tungsten wire of 5 μm in diameter. This wire was operated on a constant temperature circuit (Dantec Streamline) at an overheat ratio of 1.8. The signal from the hot wire is filtered at a cutoff frequency of 3 kHz, amplified, and then digitized using a 16-bit A/D board at a sampling frequency of 6 kHz. The record duration is 100 s for each test case. The hot wire was calibrated at the jet exit in the absence of control using a Pitot tube connected to a micromanometer (Furness Controls FCO510). The experimental uncertainty of the hot-wire measurement was estimated to be less than 2%. The centerline jet velocity U_{5D} at $x/D = 5$ was monitored with another hot wire. The decay rate of the centerline mean velocity was estimated by

$$K = (\overline{U_j} - \overline{U_{5D}})/\overline{U_j}. \tag{2}$$

A Dantec standard PIV system was used for both flow visualization and velocity field measurements. A TSI oil droplet generator (TSI MCM-30) is used to generate smoke for seeding flow. The seeding particles have a diameter of approximately 1 μm. Smoke-seeded flow was illuminated

by a laser sheet generated from two standard pulsed laser sources of 532 nm in wavelength with a maximum energy output of 30 mJ per pulse. Each laser pulse lasts for 0.01 μs. Flow images were captured at a sampling rate of 450 Hz using a charge-coupled device camera (PhantomV641, double frames, with a resolution of 2560 $\times$ 1600 pixels). A Dantec flow map processor was used to synchronize flow illumination and image capturing in the sampling process.

For PIV measurements, the captured image covers an area of $x/D \in [0, 9]$ and $y/D \in [-3, 3]$ in the injection (x, y) plane, and an area of $y/D \in [-1.5, 1.5]$ and $z/D \in [-1.5, 1.5]$ in the cross-section (y, z) plane at $x/D = 3$. The longitudinal and lateral image magnifications are identical, i.e., 0.094 mm/pixel. Following Alkislar et $al.$ [13], the time interval (50 μs) between two consecutive laser pulses was chosen to determine the maximum particle displacement of about 5 pixels. In postprocessing, a built-in adaptive correlation function of the flow map processor (Dynamic Studio software) is used with an interrogation window of 16 $\times$ 16 pixels and a 75% overlap along both directions, thus producing 160 $\times$ 100 velocity vectors. A total of 1200 pairs of flow images are captured for each set of PIV data. The percentage variations of $\bar{U}$ and $\bar{V}$ converge with the increasing number of images to less than $\pm$1% once the image number exceeds 900. As such, 1200 images are considered to be adequate for capturing the mean velocity fields.

In flow visualization measurements, the main jet was seeded with the same particles as the PIV measurements with a larger density, thus providing a clear picture for the flow structure. A total of 300 flow images are captured in each case.

C. Real-time system

A National Instrument PXIe-6356 multifunction I/O device, connected to a computer, was used in experiments for the real-time control at a sampling rate of $f_{RT} = 1$ kHz. A LABVIEW Real-Time module was used to execute the control command, e.g., the on/off mode of electromagnetic valve. Commanding actuation is performed at the same sampling rate (1 kHz). The effective excitation frequency f_a is given by $f_a = f_{RT}/N_{sp}$, where N_{sp} is the number of sampling points in one actuation period $1/f_a$. The working frequency range of actuators ([0, 500] Hz) imposes a minimum value of 2 for N_{sp}. For a given f_a, the possible duty cycle α can be deduced from $\alpha = i/N_{sp}$, $i = 1, 2, \ldots, N_{sp} - 1$. Apparently, the number of possible duty cycles N_{sp} decreases with f_a.

III. RESULTS AND DISCUSSION

A. Initial conditions of jet flow under control

In this section, the effect of the minijet on main jet exit conditions is documented. The instantaneous velocity of a single radial minijet is first examined without main jet. A hot wire was placed 17 mm upstream of the main jet exit and 3 mm radially from the exit of the minijet [Fig. 1(c)]. The hot wire was oriented normally to the minijet axis to measure the actuation velocity U_a at $\dot{m}_{mini} = 0.1$ L/min with α varied from 0.08 to 1 (Fig. 2). For $\alpha = 0.08$, U_a displays sharp periodic peaks These peaks are less pronounced at $\alpha = 0.3$ and 0.7. U_a is essentially steady at $\alpha = 1$, although displaying a small variation, as observed by Johari et $al.$ [34]. A small α produces a large instantaneous velocity, implying a large penetration depth into the main jet. It is worth mentioning that the maximum velocity U_{max} at any α is lower than $\overline{U_j}/\alpha$. For example, at $\alpha = 0.08$, $U_{max} = 5.5$ m/s, yet $\overline{U_j}/\alpha = 13.3$ m/s. The observation suggest that the actual duty cycle experienced in excitation may be slightly larger than the input duty cycle, suggesting the need for correction, which is discussed in Sec. 3 C.

An investigation is also conducted to understand the effect of C_m on $u_{rms}/\overline{U_j}$. Figure 3(a) and 3(b) present the distributions of $u_{rms}/\overline{U_j}$ at $x/D = 0.05$ along both y and z axes. In the unforced jet, $u_{rms}/\overline{U_j}$ displays a small peak at $z/D \in \pm[0.4, 0.5]$, apparently due to the rolling up of the shear-layer structures near the nozzle exit. At $C_m = 1.2\%$, $u_{rms}/\overline{U_j}$ becomes larger at $y/D \in [-0.6, -0.4]$, with a maximum of 0.06, 2.4 times that of the unforced jet. The fluctuation in the shear layer is enhanced by the minijet excitation, which accelerates the rolling up of the shear layer [35], thus
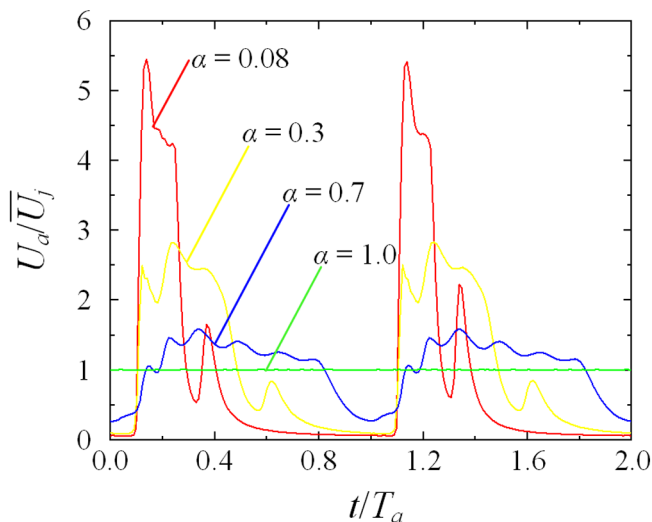
FIG. 2. Time histories of minijet injection velocity U_a at duty cycles $\alpha = 0.08$, 0.3, 0.7, and 1.0 in the absence of the main jet measured at $(x/D,\ y/D,\ z/D) = (-0.85,\ -0.4,\ 0)$ for $f_a/f_0 = 0.5$ at $\dot{m}_{\mathrm{mini}} = 0.1$ L/min.

promoting the early formation of the coherent structures. The fact that $u_{\mathrm{rms}}/\overline{U_j}$ changes little at $z/D = 0$ and $y/D \geqslant 0$ suggests that the minijet-induced strong velocity disturbance is limited to the region $y/D \leqslant 0$. As C_m increases to 1.8%, $u_{\mathrm{rms}}/\overline{U_j}$ displays a large increase at $y/D = 0$, suggesting that the minijet has penetrated through the main jet center, although leaving the shear layer at $y/D >$
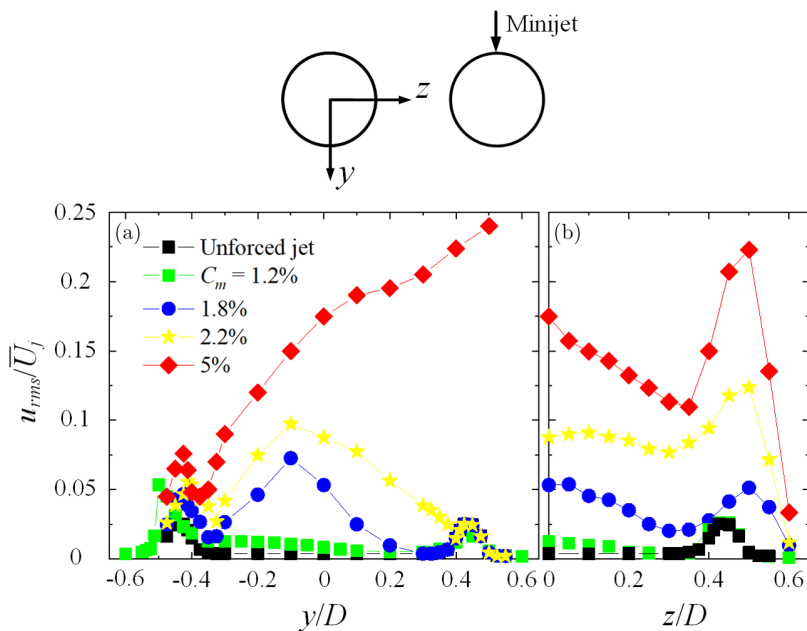
FIG. 3. Radial distributions of the fluctuating velocity $u_{\mathrm{rms}}/\overline{U_j}$ measured at $x/D = 0.05$ ($f_a/f_0 = 0.5$): (a) along the y axis and (b) along the z axis.
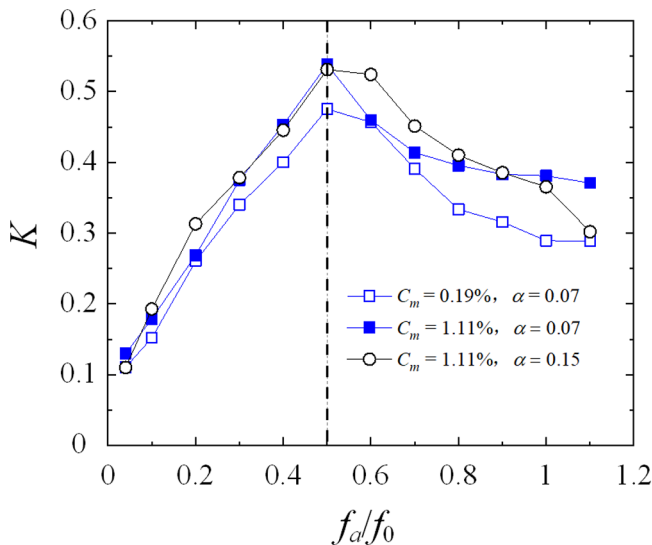
FIG. 4. Dependence on actuation frequency ratio f_a/f_0 on the jet centerline mean velocity decay rate K varied with mass-flow rate ratio C_m and duty cycle α.

0.3 undisturbed. The $u_{\text{rms}}/\overline{U_j}$ rises further at $y/D = 0$ and $0 \leqslant z/D \leqslant 0.6$ at $C_m = 2.2\%$. At $C_m = 5.0\%$, $u_{\text{rms}}/\overline{U_j}$ climbs sharply at $y/D \geqslant -0.4$ and keeps rising all the way to $y/D = 0.5$. Evidently, the minijet flow has impinged upon the opposite wall of the main jet nozzle, generating strong turbulence even before jet issues from the nozzle exit. On the other hand, $u_{\text{rms}}/\overline{U_j}$ along the z axis barely changes at $C_m = 1.2\%$ but rises substantially throughout the examined z range for $C_m \in [1.8\%, 5.0\%]$. This observation also suggests that the minijet has reached or even impinged upon the opposite wall of the nozzle for $C_m \geqslant 1.8\%$. Hence, the velocity fluctuation propagated to the orthogonal plane [Fig. 3(b)].

B. Effect of control parameters on main jet

Figure 4 presents the dependence of the decay rate K on f_a/f_0 for varied C_m and a. The K of the controlled jet exceeds that (0.05) of the natural jet over the measured range of f_a/f_0, suggesting an effective manipulation. Its value exhibits a dependence on f_a/f_0, and typically shows its peak at $f_a/f_0 = 0.5$ ($f_a D/\overline{U_j} = 0.23$), close to the Strouhal number of the "preferred mode" which is about 0.3 [36]. Freund *et al.* (2000) [18] conducted a direct numerical simulation of jet at Re = 3600, manipulated by two antiphased slot jets separated by 180° at $f_a/f_0 = 0.5$ and 1 for $C_m = 3.5\%$. They observed that the jet produced a higher spreading and reduced the length of the potential core at $f_a/f_0 = 0.5$ as compared to $f_a/f_0 = 1$, indicating the subharmonic excitation was more effective than that at the preferred-mode frequency. At $\alpha = 0.07$, the maximum K of $C_m = 1.11\%$ is larger than that of $C_m = 0.19\%$ since a large mass flow generates a large injection velocity. At $C_m = 1.11\%$, the maximum K at $\alpha = 0.15$ is less than that at $\alpha = 0.07$. This behavior is due to the fact that a small duty cycle yields a large injection velocity for a given flow rate (Fig. 2) and hence a deep penetration depth.

The K exhibits a strong dependence on C_m and α (Fig. 5). Several observations can be made. First, for all α the dependence of K on C_m ($f_a/f_0 = 0.5$) is qualitatively the same and can be divided into two categories: a rapid rise to a local maximum K followed by a drop with increasing C_m. Second, for a given small C_m, K is much larger for $\alpha = 0.1$ than for other α's, suggesting that a smaller α is more efficient in enhancing mixing. However, this trend may be reversed at C_m exceeding the maximum K. Once the penetration depth reaches the maximum, a further increase in C_m produces
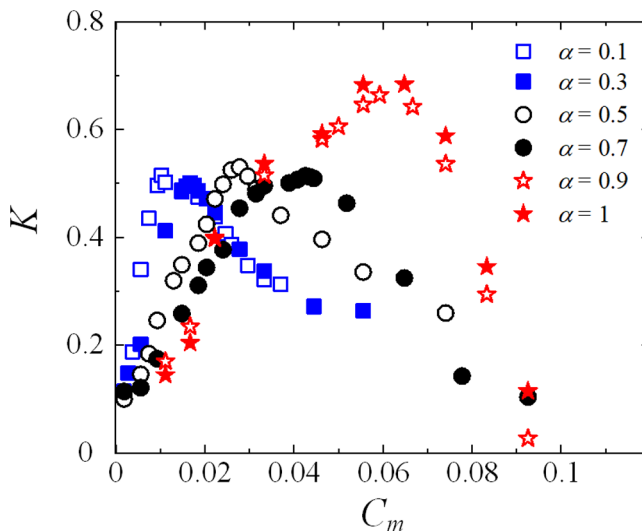
FIG. 5. Dependence on mass-flow rate ratio C_m on the jet centerline mean velocity decay rate K varied with duty cycle α.

the opposite effect, that is, the minijet impinges upon the opposite wall of the nozzle and produces turbulence, which adversely affects the development of coherent structures, causing a drop in K. Finally, C_m corresponding to the maximum K varies for different α's. A larger $\alpha (\geqslant 0.7)$ corresponds to a greater C_m and also a greater local maximum K. Given the diameter of minijet, the large C_m is associated with a large mass flow $\dot{m}_{\text{mini}}$ and injection velocity $\overline{U_a}$ [25]. As such, the momentum $(\dot{m}_{\text{mini}}\overline{U_a})$ is enhanced and hence the strength of jet column deflection is increased, which will be discussed in Sec. IV.

C. Corrected momentum ratio and jet decay rate

As is clear in Fig. 5, the dependence of K on C_m $(f_a/f_0 = 0.5)$ is qualitatively the same, irrespective of α. Given the same C_m, the maximum minijet velocity increases as α is reduced (Fig. 2). Physically, the penetration depth of the minijet is determined by the combined effect of $\dot{m}_{\text{mini}}$ and α. Note that C_m/α is physically the momentum ratio per pulse of injection of the minijet to the main jet [25]. Therefore, this momentum ratio plays an important role in the effectiveness of jet manipulation. Once replacing the abscissa in Fig. 5 by C_m/α, we see a reasonably good collapse in K in region I for various α (Fig. 6), reconfirming Perumal and Zhou's [25] finding that C_m/α is the scaling factor. However, the dependence of K on C_m/α displays a rather large scatter in region II. Furthermore, the maximum K corresponding to various α varies considerably, rising markedly for $\alpha \geqslant 0.9$. As noted by Perumal and Zhou [25], the minijet may act to deflect the main jet given a large duty cycle, which may lead to an artificially enlarged K value, as highlighted by a circle in Fig. 6.

The exit velocity of the minijet may have a significant influence on the flow structure development [21]. As such, hot-wire measurements were carried out with predetermined minijet flow rate in the absence of the main jet at a sampling frequency of 6 kHz for 100-s test time. A calibrated hot wire was placed at the minijet exit ($x/D = -0.85$, $y/D = 0$, $z/D = 0.45$) to measure its velocity. Figure 7 shows the velocity ratio $U_{a,\text{max}}/(\overline{U_a}/\alpha)$ for $\dot{m}_{\text{mini}} = 0.1, 0.2, 0.4, 0.6$, and 0.8 L/min, where $U_{a,\text{max}}$ is the measured maximum velocity. The velocity ratio is close to 1 when $\alpha \geqslant 0.5$, suggesting that the calculated maximum instantaneous velocity $\overline{U_a}/\alpha$ is equal to $U_{a,\text{max}}$. However, the velocity ratio drops rapidly as α decreases, indicating that the measured velocity is less than the predicted probably because of the choking effect [25,37]. As such, we define an effective or corrected duty
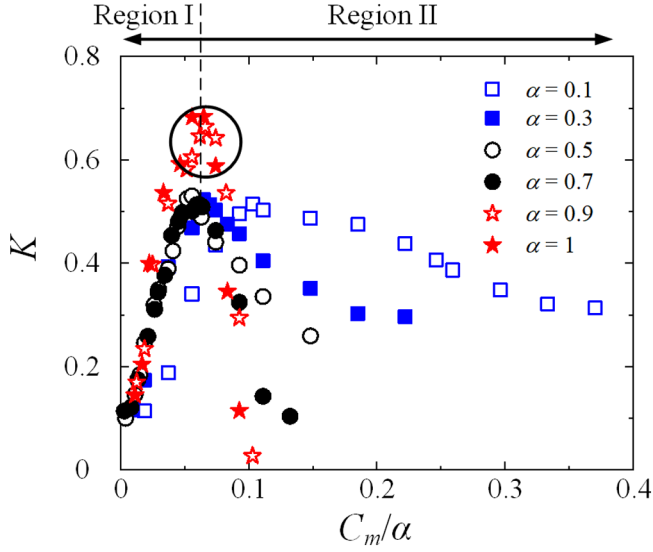
FIG. 6. Dependence on C_m/α on the jet centerline mean velocity decay rate K varied with duty cycle α.

cycle α^c:

$$\alpha^c = \overline{U_a}/U_{a,\max}. \tag{3}$$

As shown in Fig. 8, with $\overline{U_a}/\alpha$ replaced by $U_{a,\max}$, α and α^c may be correlated by

$$\alpha^c = \begin{cases} 0.725\alpha + 0.136 \text{ for } \alpha \in [0.1,\ 0.5] \\ \alpha \text{ for } \alpha \in [0.5,\ 1] \end{cases}. \tag{4}$$
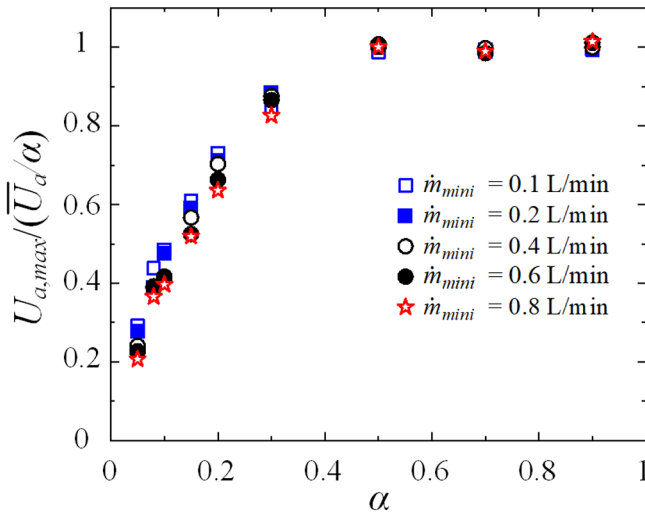
FIG. 7. Dependence on duty cycle α of $U_{a,\max}/(\overline{U_a}/\alpha)$, i.e., the ratio of the measured maximum instantaneous velocity $U_{a,\max}$ to the calculated maximum velocity $\overline{U_a}/\alpha$ for different minijet mass-flow rates $\dot{m}_{\mathrm{mini}}$.
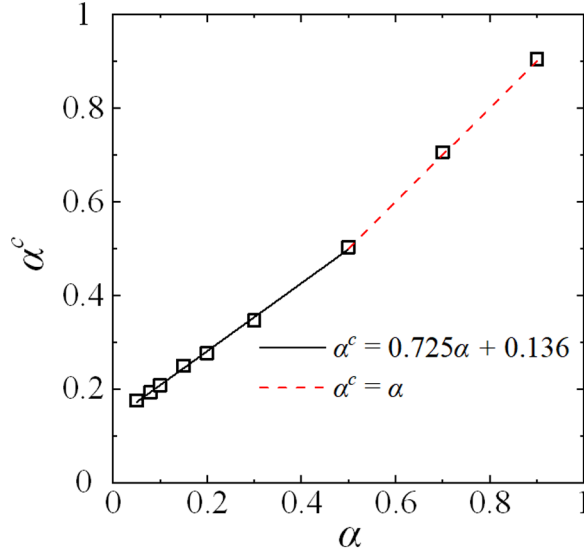
FIG. 8. Relationship between effective duty cycle $\alpha^c = \overline{U_a}/U_{a,\mathrm{max}}$ and input duty cycle α.

How the main jet responds to a variation in C_m for a given α is investigated. Figure 9 presents the normalized velocity profiles measured at $x/D = 5$ in the (x, y) plane, where a vertical solid line marks the geometric center of the unforced jet at $y/D = 0$. These profiles display five patterns, regardless of α. For instance, at $\alpha = 0.5$ [Fig. 9(c)], a single peak occurs at the jet center when $C_m \leqslant$ 1.1%, suggesting a nearly symmetric monomodal behavior, referred to as monomodal I. Please refer to the gray-colored profiles. When C_m exceeds 1.1%, the peak shifts away from the center, as highlighted by yellow color, showing a deflected jet or deflection I. The profiles, as highlighted in red, are bimodal or bifurcated when C_m is increased to 2%. As C_m increases to 2.8%, the maximum velocity (see the green-colored profiles) moves away from the center again, that is, the jet column deflects again along the minijet injection direction, known as deflection II. When C_m exceeds 5.6%, the minijet brings the maximum of the velocity profile (blue color) back to the center, that is, the main jet is aligned with its geometric centerline, called monomodal II.

Now let us consider correcting the overestimated K at $\alpha \geqslant 0.9$ in Fig. 6. Define a corrected K by

$$K^c = (\overline{U_j} - \bar{U}_{5D,\mathrm{max}})/\overline{U_j}, \tag{5}$$

where $\bar{U}_{5D,\mathrm{max}}$ denotes the maximum velocity measured at $x/D = 5$ in the (x, y) plane (Fig. 9). Then, replacing K and α in Fig. 6 by K^c and α^c leads to considerably improved collapse in the data (Fig. 10), especially in region I and the maximum K^c. However, the scattering beyond C_m/α^c at which the maximum K^c occurs remains large, albeit shrinking considerably compared to Fig. 6. The K^c in region II tends to drop with increasing α because of the choking effect.

The injected flow through the minijet nozzle of very small diameter may be partially choked at a large C_m [25], implying that the nominal mass-flow rate measured by the mass-flow meter could be overestimated [30]. In order to determine the actual mass-flow rate, we used a calibrated hot wire to measure the minijet exit velocity $\overline{U_a}$. Then, the actual mass flow can be estimated from $C_m^c = \overline{U_a}S_{\mathrm{mini}}/\dot{m}_j$, where S_{mini} denotes the area of minijet exit. Figure 11 shows C_m against C_m^c, which displays an approximate linear relationship at different duty cycles. However, the slope becomes appreciably smaller than unity for $\alpha < 0.9$, that is, C_m^c is indeed smaller than C_m. Further, the deviation grows with decreasing α.

Once we replace C_m in Fig. 10 by C_m^c, the data in region II collapse together, as shown in Fig. 12, and can be least-square fitted to $K^c = -4.516\xi^c + 0.549$, where $\xi^c = C_m^c/\alpha^c$ is physically
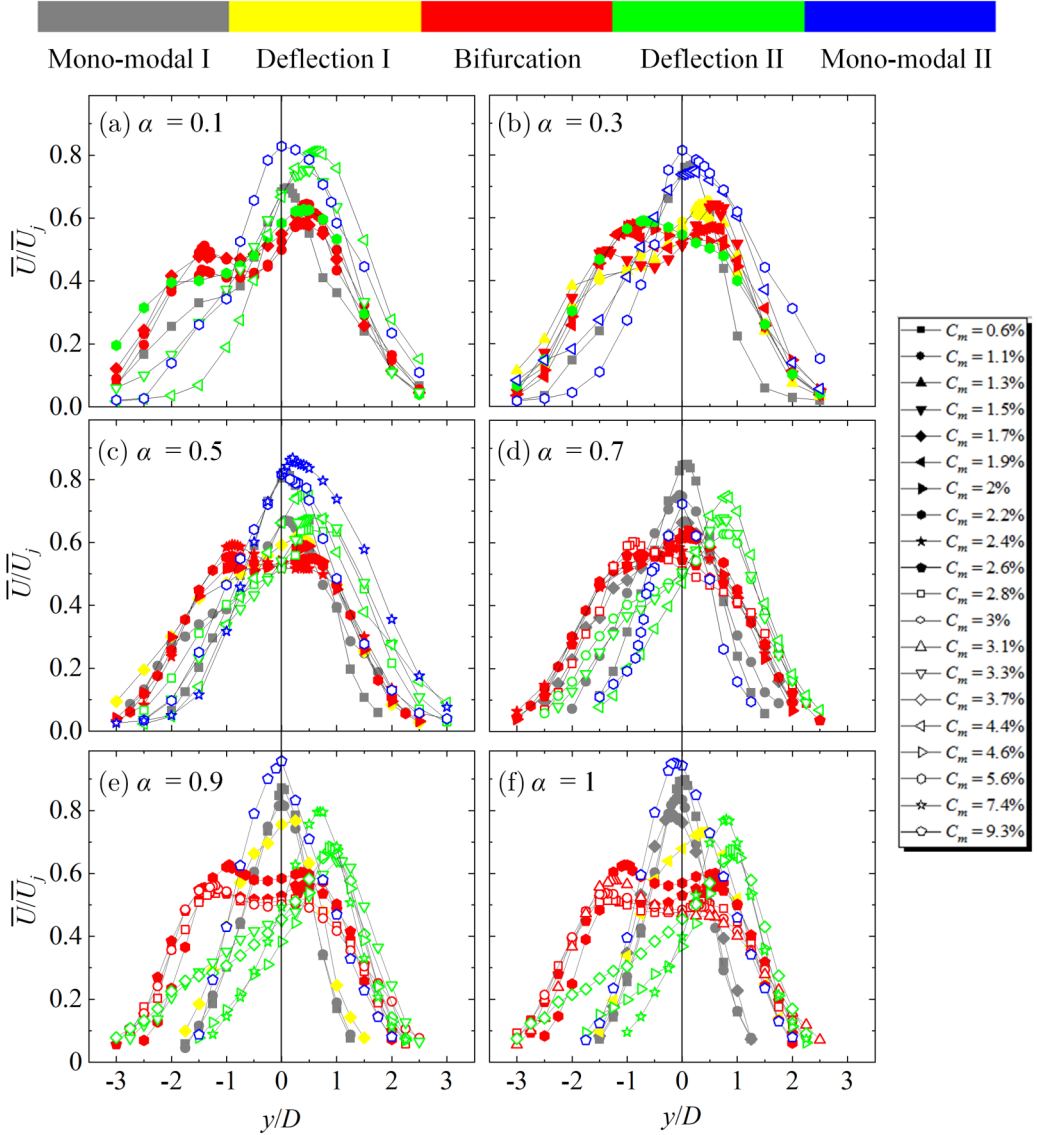
FIG. 9. The streamwise mean velocity profiles $\overline{U}/\overline{U_j}$ of the controlled jet along y axis ($x/D = 5$). The color of symbol denotes the classification of velocity profiles.

the effective momentum ratio per pulse of injection of the minijet to the main jet. For the purpose of comparison, we have also included Perumal and Zhou's [25] data (their figure 22) on the correlation between K and $\xi = \frac{\sqrt{MR}}{\alpha}(\frac{d}{D})^n$ in the figure. The dependence of K on ξ is in good agreement with that of K^c on ξ^c in region I. However, there is a marked difference in how K or K^c would vary after reaching their maxima, i.e., in region II, between the two sets of data. The $K-\xi$ correlation displays four branches, i.e., B1, B12, B2, and B3, but the $K^c-\xi^c$ data fall around a straight line. Interestingly, we arbitrarily take four points from each branch of Perumal and Zhou's [25] data, as indicated by half-solid symbols in Fig. 12, and correct C_m, α, and K. Following the previous procedures to measure $\overline{U_a}$, $U_{a,\max}$, and the cross-flow velocity profiles (Fig. 9), the obtained K^c and ξ^c fall around the line $K^c = -4.516\xi^c + 0.549$, as highlighted by pink color.
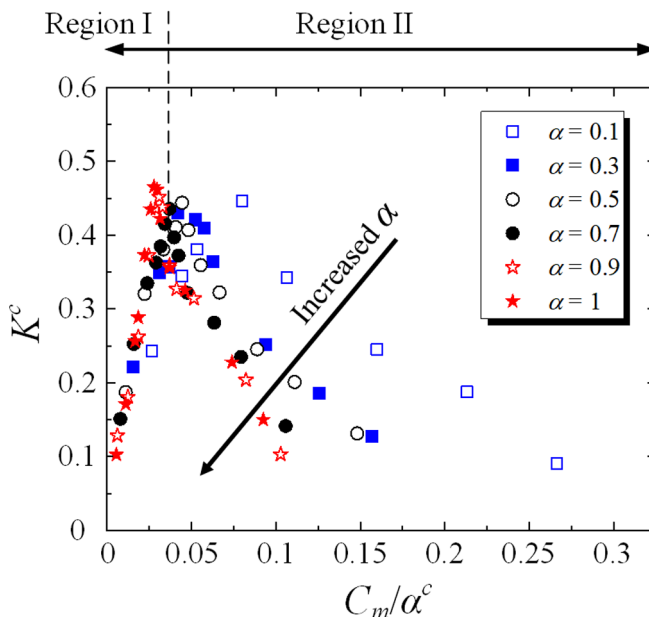
FIG. 10. Dependence on C_m/a^c on the corrected jet centerline mean velocity decay rate K^c varied with duty cycle.

D. Discussion

Figure 13 presents the dependence of the flow pattern on $K^c - \xi^c$ and the corresponding photographs of flow visualization images. We see five distinct flow patterns, corresponding to monomodal I, deflection I, bifurcation, deflection II, and monomodal II. Monomodal I corresponds to the single peak of the velocity profile ($\xi^c = 0.004$–0.012), where the peak occurs at the centerline
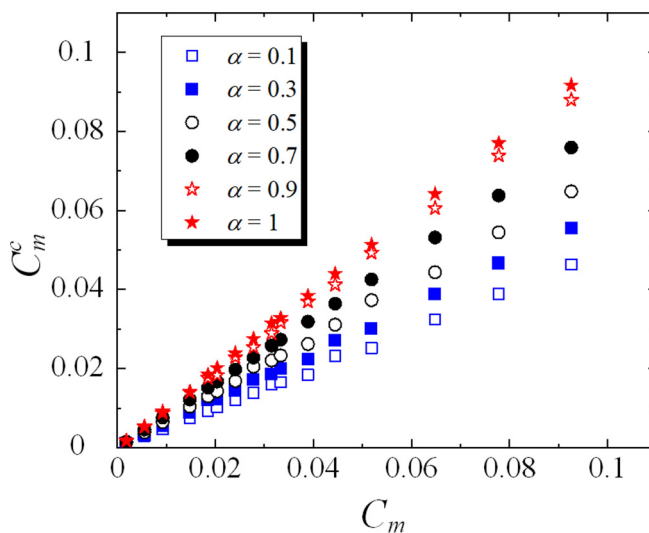
FIG. 11. Dependence on effective mass-flow rate C_m^c on the nominal mass-flow rate C_m varied with duty cycle.
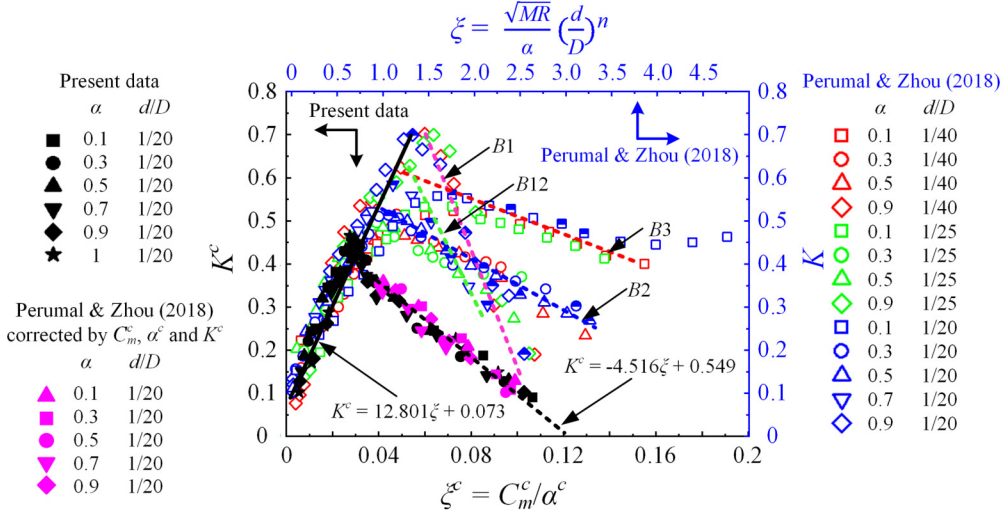
FIG. 12. Dependence on effective momentum ratio $\xi^c = C_m^c/\alpha^c$ on the corrected jet centerline mean velocity decay rate K^c varied with duty cycle. Note that the data from Perumal and Zhou [25] are also included. The decay rate of the blue half-solid symbol is remeasured and replotted with pink.

and the minijet produces little disturbance to the opposite side coherent structures. Please refer to the green color profile in Fig. 13(a). From $\xi^c = 0.013$–0.021, deflection I occurs between monomodal I and bifurcation regions. This flow structure is characterized by a deflected jet column. The jet column moves away from the jet centerline along the minijet actuation direction [Fig. 13(b)]. With ξ^c increasing further to 0.031 [Fig. 13(c)], the velocity profile displays two peaks, indicating the occurrence of a bifurcating jet or bimodal behavior [38]. When actuated by the minijet actuation intensely, the minijet penetration depth becomes large and even exceeds the centerline of the main jet, thus resulting in a flapping motion downstream and rapid mixing with ambient fluid. Deflection II takes place at $\xi^c = 0.038$–0.066, which is connected to the deflected flow. Compared with deflection I, the transversally deflected velocity profile is significantly broadened [Fig. 13(d)]. When ξ^c exceeds 0.066, the monomodal II takes place, which is characterized by a broad velocity profile with a single maximum located at the geometrical center [Fig. 13(e)].

Flow visualization experiment was conducted in the (x, y) plane for all five patterns of the manipulated jet in order to gain further understanding of the flow physics (Fig. 13). There is a profound change in the flow structure with and without excitation and even between different patterns under excitation. As a reference, the flow structure of the unforced jet is also given in Fig. 13(u), where the shear layer rolls up, forming a ring vortex at $x/D \approx 2$ due to the Kelvin-Helmholtz instability. The vortices grow as moving downstream, engulfing ambient fluid (black-colored) into the jet core when becoming fully turbulent. Once perturbed at $\xi^c = 0.008$, the coherent structure on the upper side of the main jet appears undisturbed since the minijet penetration depth is small, not going beyond the centerline, as is evident by the u_{rms} distribution at $C_m = 1.2\%$ in Fig. 3. The maximum value of the velocity profile stays on the geometric centerline [Fig. 13(a)]. Perumal and Zhou [25] made a similar observation at $C_m = 0.2\%$ and $\alpha = 0.7$ and 0.9 (see their figure 14e,f). When the control jet is activated at the effective momentum ratio $\xi^c = 0.016$, the jet column displays a deflection, as indicated by the white arrow in Fig. 13(b), similarly to jet vectoring by Tamburello and Amitay [39] who used a single synthetic jet at a 30°angle with respect to the centerline of the main jet. For the case of bifurcation ($\xi^c = 0.031$), two typical instantaneous states take place. Figure 13(c1) and 13(c2) presents the jet column moving up at one instant but down at another. The distribution of the velocity shows two peaks. As ξ^c is increased to 0.047, the maximum velocity of the profile
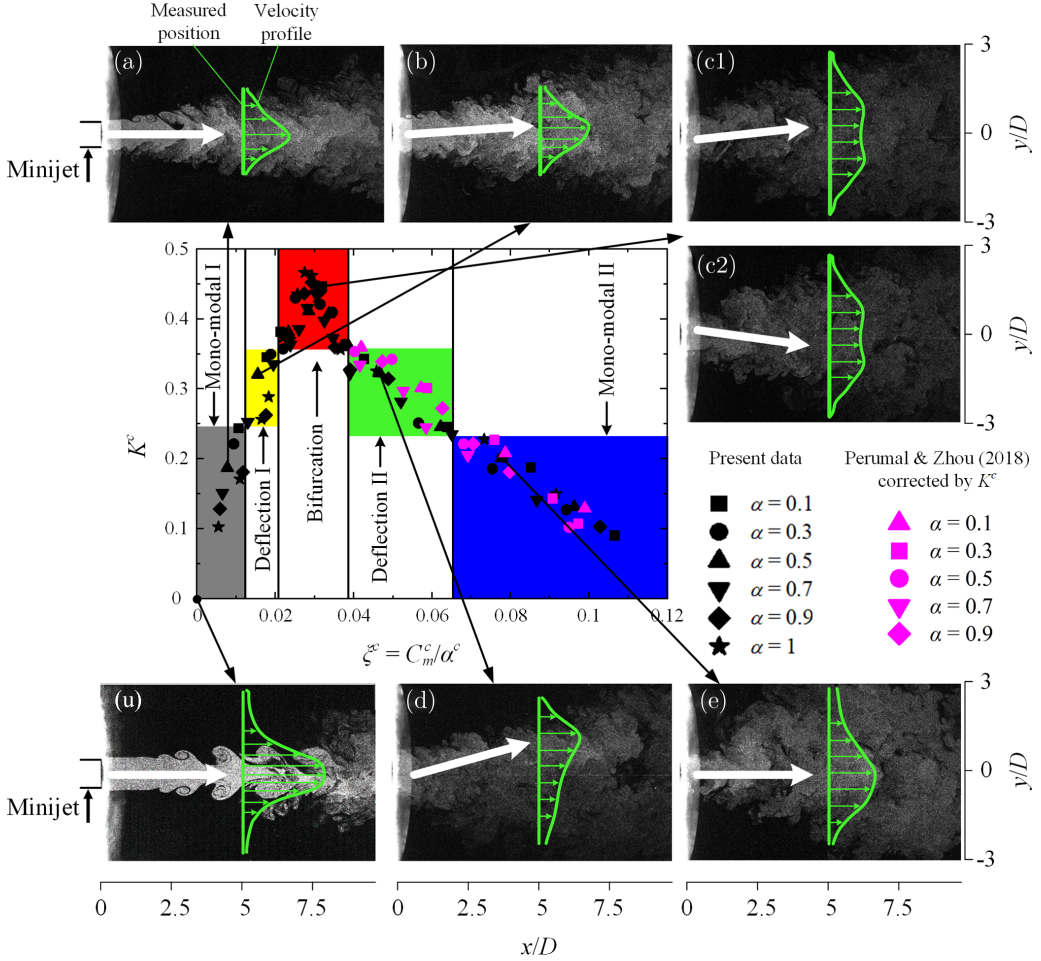
FIG. 13. Dependence of K^c and corresponding flow patterns on effective momentum ratio $\xi^c = C_m^c/\alpha^c$. Each colored area indicates one type of flow structure; gray, yellow, red, green, and blue represent monomodal I, deflection I, bifurcation, deflection II, and monomodal II, respectively. The green curves and white arrows in each subfigure indicate the velocity profile measured at $x/D = 5$ and jet column deviating from the centerline, respectively.

occurs off the centerline and the jet column is again vectored along the minijet injection due to a large penetration depth of the minijet, resulting in an increased deflection angle and spreading area [Fig. 13(d)]. As a consequence, there is an artificial increase in K. When ξ^c is equal to 0.078, Fig. 13(e) shows a further broadened main jet, which exhibits a single-peak or monomodal velocity distribution.

To understand further the predominant flow structures under the five types of forcing in Fig. 14, we examine time-averaged $\bar{U}/\overline{U_j}$ and $\bar{V}/\overline{U_j}$ in the (x, y) plane based on the PIV data. For $\xi^c = 0.008$, the $\bar{U}/\overline{U_j}$ contours exhibit a nearly symmetric distribution along the y axis and the potential core contracts to $x/D = 4.5$ [Fig. 14(a1)]. The $\bar{V}/\overline{U_j}$ contours also show a symmetric distribution [Fig. 14(a2)]. For deflecting jet with $\xi^c = 0.016$, the $\bar{U}/\overline{U_j}$ contours exhibits a symmetric distribution along the y axis when $x/D \leqslant 4$, while the maximum $\bar{U}/\overline{U_j}$ concentration moves outward to the positive y [Fig. 14(b1)]. The maximum $\bar{V}/\overline{U_j}$ is about 0.23 when $y/D \geqslant 0$, larger than the maximum
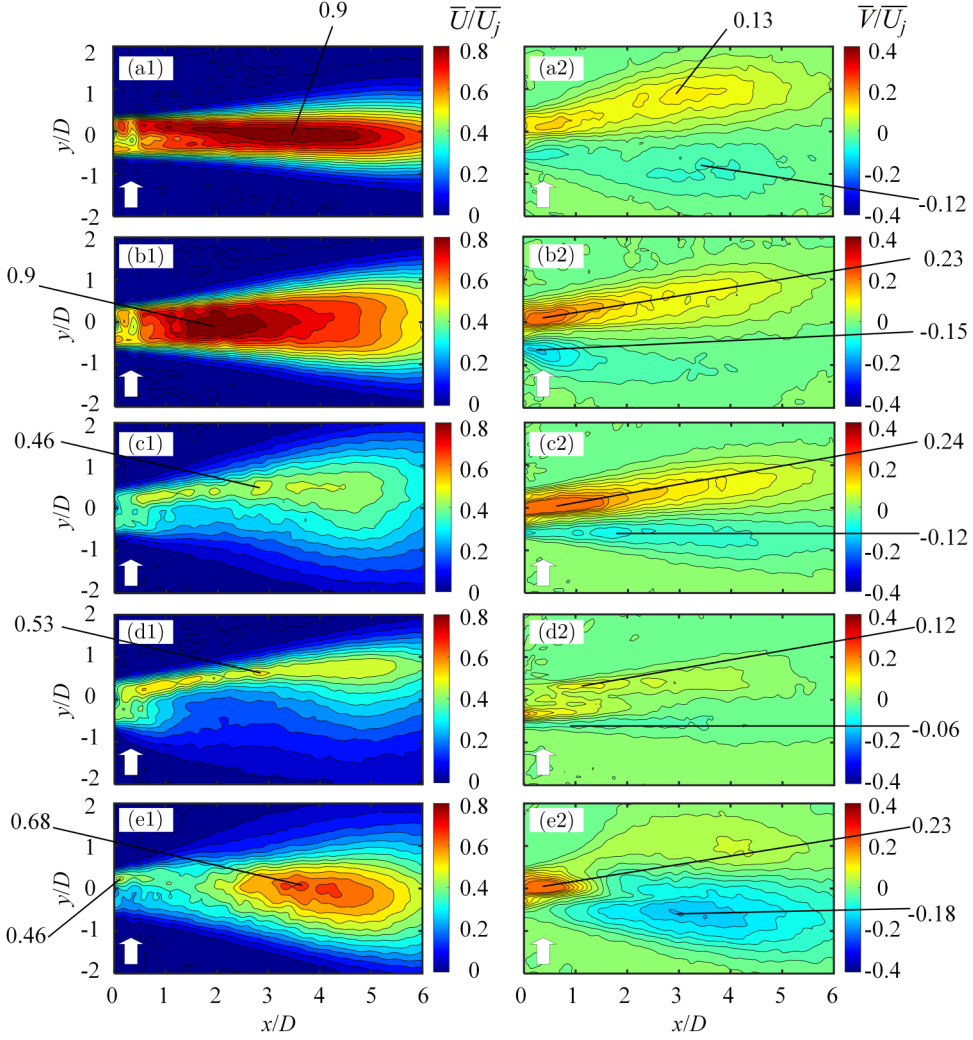
FIG. 14. Isocontours of mean velocities $\bar{U}/\overline{U}_j$ (left column) and $\bar{V}/\overline{U}_j$ (right column) in the (x, y) plane: (a) monomodal I ($\xi^c = 0.008$), (b) deflection I ($\xi^c = 0.016$), (c) bifurcation ($\xi^c = 0.031$), (d) deflection II ($\xi^c = 0.047$), and (e) monomodal II ($\xi^c = 0.078$). Contour interval = 0.05 for $\bar{U}/\overline{U}_j$. Contour interval = 0.025 for $\bar{V}/\overline{U}_j$. The white arrows denote the minijet injection.

magnitude of $\bar{V}/\overline{U}_j$ (-0.15) when $y/D \leqslant 0$ [Fig. 14(b2)]. The results are internally consistent with the observed deflected jet. For the bimodal behavior, when the main jet is actuated at $\xi^c = 0.031$, the maximum magnitudes of $\bar{V}/\overline{U}_j$ reach 0.24 and 0.12 above and below the centerline, respectively [Fig. 14(c2)], which exceed their counterparts of monomodal I and deflection II, but are comparable to monomodal II and deflection I. However, the maximum velocity $\bar{U}/\overline{U}_j$ drops to 0.46 on the center of the jet column [Fig. 14(c1)], smaller than other cases, implying that the excitation gives rise to a maximum drop in the potential core length. When ξ^c is large, say reaching 0.047, the main jet is deflected away, as shown in Fig. 14(d1). This is also noticeable in the $\bar{V}/\overline{U}_j$ contours [Fig. 14(d2)], which are topologically different from Fig. 14(c2), as the negative contours are almost invisible in Fig. 14(d2). At the highest $\xi^c = 0.078$, the jet grows significantly in width. The maximum $\bar{U}/\overline{U}_j$ is about 0.46 near the exit, less than that (0.68) at $x/D \approx 4$ [Fig. 14(e1)]. Furthermore, the

maximum positive velocity $\bar{V}/\overline{U_j}$ (0.23) near the main jet exit is further increased [Fig. 14(e2)], while the maximum magnitude (-0.18) of negative $\bar{V}/\overline{U_j}$ occurs downstream. The jet column is approximately aligned with the centerline at $x/D = 5$ [Fig. 13(e)]. The observations indicate the main jet moves up along the minijet injection and then bows back downstream toward the opposite side, forming a nearly symmetric monomodal jet.

Additional insight into the differences between the five flow structures may be gained by examining the PIV and hot-wire data measured in the (y, z) plane at $x/D = 3$, with and without control. Figure 15 presents the streamwise vorticity $\bar{\omega}_x^*$ contours averaged over 1200 snapshots, and Fig. 16 shows the radial profiles of the hot-wire measured $\bar{U}/\overline{U_j}$ at $x/D = 3$ in both (x, y) and (x, z) planes. For monomodal I ($\xi^c = 0.008$), the minijet injection depth is small, giving rise to only small vorticity concentrations [Fig. 15(a)] scattered around the jet core [cf. Fig. 15(u)]. As such, the corresponding streamwise mean velocity profile is almost symmetrical about y/D or $z/D = 0$, with its maximum at the center (Fig. 16). For deflection I, the increased penetration depth ($\xi^c = 0.016$) induces one pair of streamwise counter-rotating vortices about the minijet exit. The two vortices induce another pair of vortices, which occur farther away from the injection point and are weaker in terms of the size and vorticity magnitude [Fig. 15(b)]. Following Jiménez-González et al. [40], each pair of streamwise counter-rotating vortices may induce one positive streamwise streak, whose possible location is indicated by the elliptic contour in Fig. 15(b). As a matter of fact, the occurrence of two streamwise streaks may account for the relatively broad streamwise velocity profile in Fig. 14(b1) [cf. Fig. 14(a1)]. As a result, the lateral velocity $\bar{V}/\overline{U_j}$ in the (x, y) plane is markedly increased [Fig. 14(b2); cf. Fig. 14(a2)], showing a jet fluid motion from the bottom to top [Fig. 13(b)], and the peak in the velocity profile deviates appreciably from its geometric center [Fig. 16(a)]. In the case of bifurcation [$\xi^c = 0.031$, Fig. 15(c)], two pairs of streamwise vortices are approximately symmetric about the geometric center. Again, two positive streaks could be induced, which could interact with the forced Kelvin-Helmholtz mode, contributing to the occurrence of the bifurcated jet, as is observed in the (x, y) plane [Fig. 14(c2)]. As such, the velocity profile in the (x, y) plane exhibits a twin-peak distribution [Fig. 16(a)]. In case of deflection II ($\xi^c = 0.047$), the penetration depth triples that in Fig. 15(b) (deflection I), thus producing two pairs of streamwise counter-rotating vortices [Fig. 15(d)]. One pair with a larger maximum vorticity magnitude $\bar{\omega}_x^* = 0.9$ occurs on the right side of the jet, while the other with a maximum vorticity magnitude $\bar{\omega}_x^* = 0.4$ [Fig. 15(d)] takes place on the left. The former induces a relatively large positive streamwise streak, as indicated by $\bar{U}/\overline{U_j} = 0.53$ in Fig. 14(d1). This streak could contribute to the jet vectoring from the bottom to top [Fig. 13(d)]. Consequently, the peak of the velocity profile is deflected from the geometric center [Fig. 16(a)]. A similar observation is made numerically by Jiménez-González et al. [40] when manipulating a round jet under the helical mode ($m = 1$), who proposed a "shift-up" mechanism (see their figure 10a), that is, the radial perturbation may generate streamwise counter-rotating vortices of opposite sign near the jet exit, which develop into a dipole further downstream and generate a streamwise streak. The dipole acted to shift the entire jet radially, giving rise to axial velocity streaks which spread from the side of the round jet core to the other (see figures 10(a) and 11 in Ref. [40]). Monomodal II ($\xi^c = 0.78$) is characterized by one pair of strong streamwise counter-rotating vortices in terms of both size and maximum $\bar{\omega}_x^*$ [Fig. 15(e)], which induce a single positive streamwise streak about the jet center with a maximum $\bar{U}/\overline{U_j} = 0.68$ [Fig. 14(e1)], without causing any appreciable shift in the jet [Fig. 14(e1), Fig. 16(a)].

Some remarks are due on the role of the different azimuthal modes m in the control of a round jet. Jiménez-González et al. [40] identified two transient growth mechanisms when investigating a turbulent round jet under $m = 0$ (axisymmetric mode) and 1 (helical mode). One is the Orr mechanism, which corresponds to the reorientation of two-dimensional vortical structures initially inclined against the shear that injects energy by rearranging the vortical structures along it. Another is the shift-up effect, which shifts the entire jet due to the reorganization of the flow by streamwise counter-rotating vortices. Jet flapping is due to the excitation of the $m = \pm 1$ mode [41]. Samimy et al. [42] achieved a higher enhancement of jet mixing and a faster decay rate of jet centerline
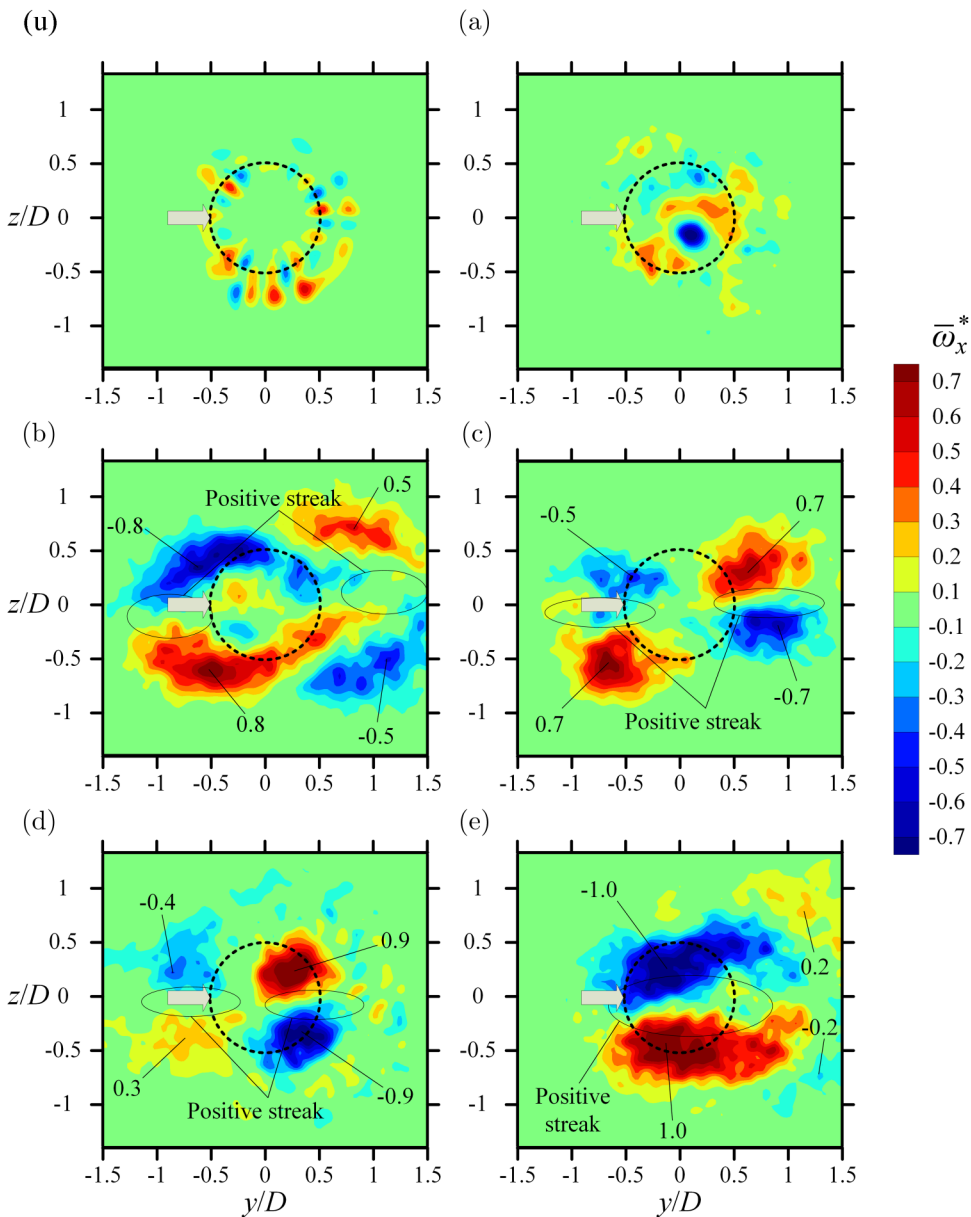
FIG. 15. Time-averaged vorticity $\bar{\omega}_x^*$-contours in the (y, z) plane of $x/D = 3$: (u) unforced, (a) monomodal I ($\xi^c = 0.008$), (b) deflection I ($\xi^c = 0.016$), (c) bifurcation ($\xi^c = 0.031$), (d) deflection II ($\xi^c = 0.047$), and (e) monomodal II ($\xi^c = 0.078$). The dotted circle, gray arrow, and elliptic contour denote the main jet exit, minijet injection, and streamwise streak induced by a pair of counter-rotating streamwise vortices, respectively.

velocity by exciting a round jet with the $m = \pm 1$ mode at the preferred-mode frequency of jet than that excited with the $m = 0$ mode at the same frequency. They observed that the structures are symmetric when excited by the $m = 0$ mode but staggered or bifurcated by the $m = \pm 1$ mode. Parekh *et al.* [41] deployed two antiphase slot jets to control a round jet under the $m = \pm 1$ mode, producing a bifurcating jet that enhanced effectively jet mixing. The round jet may bifurcate or flap when manipulated using two opposite circumferential speakers out of phase [38] or two unsteady
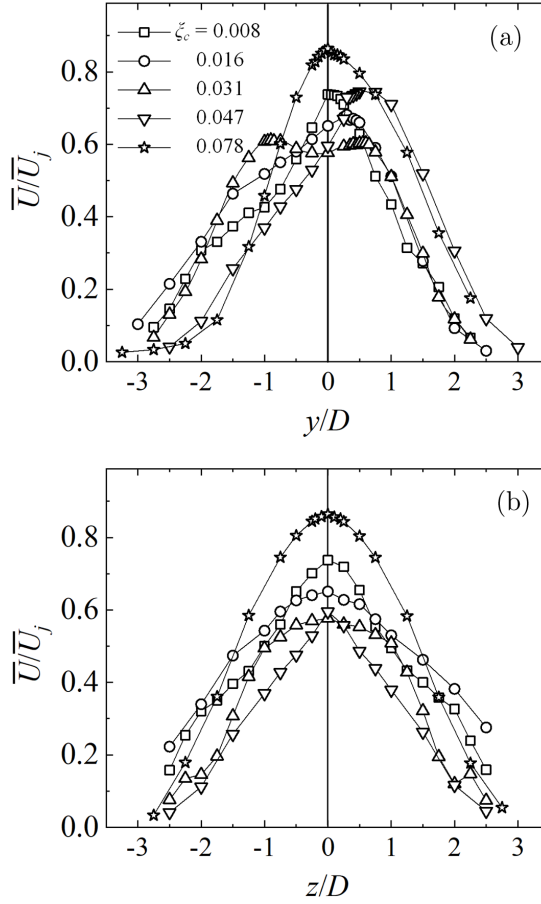
FIG. 16. Radial distributions of $\bar{U}/\bar{U}_j$ measured at $x/D = 3$ in both (x, y) and (x, z) planes for monomodal I ($\xi^c = 0.008$), deflection I ($\xi^c = 0.016$), bifurcation ($\xi^c = 0.031$), deflection II ($\xi^c = 0.047$), and monomodal II ($\xi^c = 0.078$).

minijets azimuthally separated by $60°$ [43]. The present study demonstrates that an asymmetric excitation using a single minijet may also produce the staggered vortices and a bifurcating jet.

It is worth commenting on the role the interaction between the shear-layer instability and periodic forcing plays in the development of the mean flow (Fig. 4). As recently found by Perumal *et al.* [44], the flow structure of the jet, when manipulated, depends on the effective penetration depth and the actuation frequency ratio f_a/f_0. Given an effective penetration depth, the actuation frequency ratio may dictate the development of interactions between successive vortices and hence the flow. Take $\xi^c = 0.025$ for example. Figure 17 presents typical images from flow visualization at Re = 8000 captured in the injection plane (x, y), along with the corresponding hot-wire signals or instantaneous streamwise velocity $U/\bar{U}_j$, as f_a/f_0 varies. Compared with the unforced jet [Fig. 13(u), the shear layer rolls up early on the injection side when control is applied. The perturbed coherent structures exhibit a strong dependence on f_a/f_0. Three representative states can be identified: in state 1 or the optimal state where $f_a/f_0 = 0.5$ and K achieves its maximum (Fig. 4). As shown in Fig. 17(a1), the peaks of the hot-wire signal are distinctly separated, and one coherent structure V_2 excited by one minijet injection pulse interacts optimally with the upstream coherent structure V_1 excited by the next minijet injection pulse [Fig. 17(a2)]. Note that the upper and lower coherent structures, as enclosed by the yellow-colored contour, are approximately antisymmetrically arranged about the jet
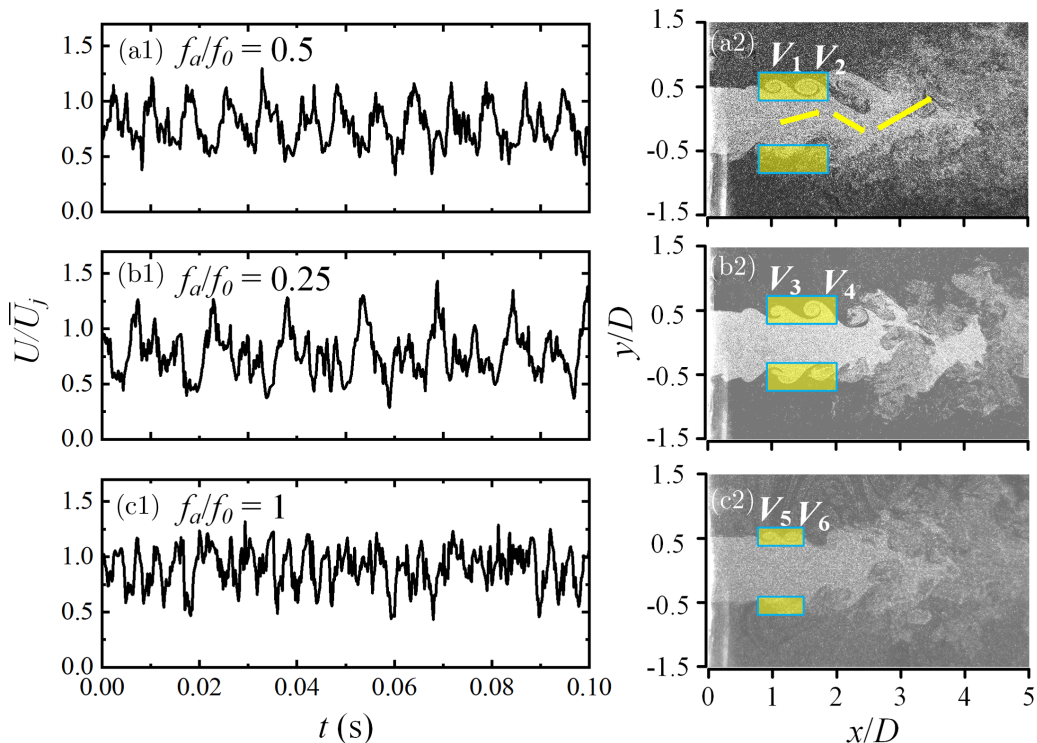
FIG. 17. (a1)–(c1) Typical instantaneous streamwise velocity $U/\bar{U}_j$ signals measured at $(x/D, y/D, z/D) = (1.5, 0, 0.45)$ for $\xi^c = 0.025$ and $f_a/f_0 = 0.5$, 0.25, and 1 at Re = 8000. (a2)–(c2) Typical flow structures from flow visualization in the injection plane (x, y) at representative f_a/f_0, where the vortices V_1–V_6 result from the minijet injection.

centerline and the jet column appears wobbling, as indicated by yellow arrows, showing the feature of a bifurcated jet. The jet bifurcation mechanism, that is, how the minijet injection induced the antisymmetrically arranged coherent structures and how the jet bifurcation was connected to the structures, is discussed in detail by Yang *et al.* [43]. State 2 corresponds to a smaller $f_a/f_0 = 0.25$ [Fig. 17(b)]. As shown in the instantaneous streamwise velocity signals [Fig. 17(b1)], two adjacent peaks display an increased gap. This increased gap leads to weakened interactions between adjacent two coherent structures, as supported by the approximately symmetric arrangement of upper and lower structures about the centerline [Fig. 17(b2)], which is a signature of the ring vortex as in an unforced jet. Correspondingly, there is a decrease in the jet decay rate (Fig. 4). For state 3 where $f_a/f_0 = 1$ [Fig. 17(c)], the peaks of the hot-wire signal are very close to each other [Fig. 17(c1)] and the spatial separation between vortices V_5 and V_6 contracts, resulting in intensive interactions between them [Figs. 17(c1)–17(c2)]. Such an interaction may incur the occurrence of turbulent pufflike structures, accounting for a reduced mixing rate [45]. As such, the jet decay rate also drops compared to state 1 (Fig. 4).

Experimental data show unequivocally that the flow structure of the manipulated main jet is linked to the effective momentum ratio. Conceptual models are thus proposed for the controlled jet at different ξ^c (Fig. 18). The minijet interacts with the main flow upstream of the nozzle exit. As a reference, the unforced jet [Figs. 18(u1)–18(u2)] is essentially potential flow near the exit, although associated with approximately axisymmetric mushroomlike structure downstream [29]. When ξ^c is 0.008, the minijet, as marked by the blue arrow, interacts with the main flow upstream of the nozzle exit. The minijet injection velocity is small and its penetration depth does not
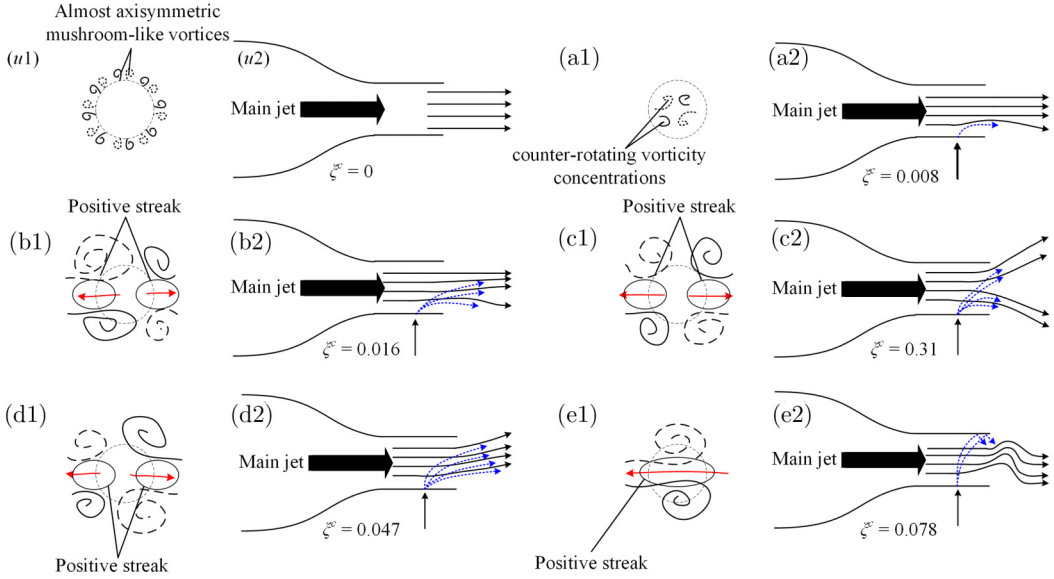
FIG. 18. Conceptual model of the flow structure for the jet manipulation by minijet at different ξ^c region: (u) unforced jet, (a) monomodal I ($\xi^c = 0.008$), (b) deflection I ($\xi^c = 0.016$), (c) bifurcation ($\xi^c = 0.031$), (d) deflection II ($\xi^c = 0.047$), and (e) monomodal II ($\xi^c = 0.078$). The black, blue, and red thin arrows denote the main jet, minijet-produced structures, and jet motion induced by the streaks (elliptic contour), respectively. The black thick arrow indicates the main jet. The solid and dashed line indicate the positive and negative vortices, respectively.

reach the centerline [Figs. 18(a1)–18(a2)]; nevertheless, it does incur two counter-rotating vorticity concentrations about the jet center [Fig. 15(a)]. As ξ^c equals 0.016, the minijet shoots beyond the centerline (blue arrow), resulting in two pairs of counter-rotating streamwise vortices and hence two positive streaks [Fig. 18(b1)], as discussed earlier, thus vectoring the main jet away from centerline [Fig. 18(b2)]. For the bimodal at $\xi^c = 0.031$, the minijet-produced structure penetrates deeper [Fig. 18(c1)], and the two pairs of streamwise vortices are now quite symmetric about the geometric center, and their induced two streaks interact with the forced Kelvin-Helmholtz mode, causing a bifurcated jet. Hence, the jet exhibits alternate upward and downward motions from $x/D \approx 2$ [Fig. 13(c)]. Asymmetrically arranged, vortex interactions entrain ambient fluid on the lower side and push the core fluid out on the upper side at $x/D \approx 2$ in Fig. 13(c1), thus producing a strong upward motion. Similarly, a strong downward motion occurs at $x/D \approx 2.5$ in Fig. 13(c2). As a result, a bifurcated jet column is generated, as schematically shown by two upper blue arrows [Fig. 18(c2)]. This is in agreement with previous investigations on the asymmetric manipulation of a jet, where asymmetric excitation may lead to asymmetrically arranged vortices [46]. Increasing ξ^c to 0.047, the minijet-produced structures penetrate the centerline of the main jet, causing the pair of counter-rotating streamwise vortices on the right considerably stronger than that on the left [Fig. 18(d1)]. The positive streamwise streak associated with the former is therefore characterized by larger strength than that induced by the latter. This difference acts to push the main jet vector away from the minijet injection point, as indicated by the black arrow [Fig. 18(d2)]. At the largest $\xi^c = 0.078$, the minijet impinges upon the opposite wall of the nozzle. As a result, the bounce-back motion was generated, as schematically shown by the blue arrows in Fig. 18(e2). This motion may enhance the generation of turbulence, disturbing the generated streamwise vortices and hence the streamwise streak, accounting for a diminished deflection.

IV. CONCLUSIONS

A systematic investigation has been carried out on the manipulation of a round jet for mixing enhancement using an unsteady radial minijet. Three control parameters are examined, i.e., C_m ($0.6 \sim 10\%$), f_a/f_0 ($0.5 \sim 1$), and α ($0.1 \sim 1$). Extensive measurements are performed in three orthogonal planes of the main jet. The following conclusions can be drawn from this investigation.

(1) Empirical scaling analysis performed on the experimental data, at $f_a/f_0 = 0.5$, unveils that the relationship $K = g_1(C_m, \alpha)$ may be reduced to $K^c = g_2(\xi^c)$, where g_1 and g_2 are two functions (Fig. 11). K^c and $\xi^c = C_m^c/\alpha^c$ are physically the corrected decay rate of jet centerline mean velocity and the effective penetration depth, respectively. This simple scaling law is obtained on the basis of several observations. First, the ratio between the maximum minijet velocity $U_{a,\max}$ and time-averaged velocity $\overline{U_a}$ is well approximated by the duty cycle α for $\alpha \geqslant 0.5$; however, this ratio deviates appreciably from α for $\alpha < 0.5$. As the minijet-on duration becomes very small for a given mass-flow rate, the minijet injection may not follow the actuation command and could exceed slightly the time window specified by the input duty cycle, as a result of remaining fluid flowing, even after the valve closure, through the tube that connects the valve and nozzle [37,47]. Thus, there is a need to introduce the effective duty cycle $\alpha^c = \bar{U}_a/U_{a,\max}$ which is found to be almost independent of C_m. Second, the effective mass-flow ratio C_m^c is introduced based on the measured averaged minijet velocity. It is found that C_m^c is identical to C_m for $\alpha \geqslant 0.9$ but becomes appreciably smaller for $\alpha < 0.9$. Third, the jet decay rate is replaced by $K^c = (\bar{U}_j - \bar{U}_{5D,\max})/\bar{U}_j$, where $\bar{U}_j$ and $\bar{U}_{5D,\max}$ are jet exit velocity and the hot-wire measured maximum streamwise velocity at the end of the potential core ($x/D = 5$) for the deflected or bifurcating jet.

(2) The manipulated jet is classified as five typical modes, i.e., monomodal I, deflection I, bifurcation, deflection II, and monomodal II (Fig. 13). Monomodal I occurs at $\xi^c = 0.004 \sim 0.012$, corresponding to $K^c = 0.10 \sim 0.24$, and is characterized by a time-averaged streamwise velocity profile symmetric about the jet center [Figs. 13(a) and 13(e)]. From $\xi^c = 0.013 \sim 0.021$, deflection I takes place and K^c rises from 0.25 to 0.35, when the velocity profile is transversally deflected, as illustrated in Fig. 13(b). With ξ^c increasing further to 0.029, K^c reaches its maximum, 0.47, and the profile exhibits a bifurcation behavior with two peaks, one on each side of the jet center [Fig. 13(c)]. As ξ^c goes beyond 0.038, not exceeding 0.066, K^c declines with an increase in ξ^c, and deflection II is observed where the transversally deflected velocity profile [Fig. 13(d)] is significantly broadened, compared with deflection I. A further increase in ξ^c leads to a smaller K^c and the velocity profile exhibits a single peak, i.e., monomodal II [Fig. 13(e)], which is characterized by a greatly broadened velocity profile with a single peak.

(3) The five typical flow structure modes have been connected, based on the experimental data, to the effective penetration depth ξ^c of the minijet or the initial interactions between the minijet and the main jet (Fig. 18). When ξ^c is very small or large, the minijet fluid remains close to the wall where the minijet issues or impinges upon the opposite wall [Figs. 18(a) and 18(e)], resulting in a nearly symmetric monomodal jet, i.e., monomodal I or II. When the minijet fluid approaches the jet center [Fig. 18(c)], the jet bifurcates, forming the bifurcation mode and the two peaks in the velocity profile. For the remaining two intermediate cases, the jet is deflected, in the direction of the minijet injection, at a small angle ($3° \sim 5°$) when the jet does not penetrate the centerline [Fig. 18(b)] or at a larger angle ($5° \sim 8°$) otherwise [Fig. 18(d)].

[1] X. Garnaud, L. Lesshafft, P. J. Schmid, and P. Huerre, The preferred mode of incompressible jets: Linear frequency response analysis, J. Fluid Mech. **716**, 189 (2013).

[2] J. Mi, M. Xu, and T. Zhou, Reynolds number influence on statistical behaviors of turbulence in a circular free jet, Phys. Fluids **25**, 075101 (2013).

[3] M. Breda and O. R. H. Buxton, Influence of coherent structures on the evolution of an axisymmetric turbulent jet, Phys. Fluids **30**, 035109 (2018).

[4] A. R. Karagozian, The jet in crossflow, Phys. Fluids **26**, 101303 (2014).

[5] P. A. Kumar, S. M. A. Kumar, A. S. Mitra, and E. Rathakrishnan, Fluidic injectors for supersonic jet control, Phys. Fluids **30**, 126101 (2018).

[6] E. Laurendeau, P. Jordan, J. P. Bonnet, J. Delville, P. Parnaudeau, and E. Lamballais, Subsonic jet noise reduction by fluidic control: The interaction region and the global effect, Phys. Fluids **20**, 101519 (2008).

[7] A. V. G. Cavalieri, P. Jordan, Y. Gervais, M. Wei, and J. B. Freund, Intermittent sound generation and its control in a free-shear flow, Phys. Fluids **22**, 115113 (2010).

[8] A. V. G. Cavalieri, P. Jordan, W. R. Wolf, and Y. Gervais, Scattering of wavepackets by a flat plate in the vicinity of a turbulent jet, J. Sound Vib. **333**, 6516 (2014).

[9] C. M. Ho and E. Gutmark, Vortex induction and mass entrainment in a small-aspect-ratio elliptic jet, J. Fluid Mech. **179**, 383 (1987).

[10] E. J. Gutmark and F. F. Grinstein, Flow control with noncircular jets, Ann. Rev. Fluid Mech. **31**, 239 (1999).

[11] T. H. New, K. S. Tan, and H. M. Tsai, Effects of noncircular collars on an axisymmetric jet, Phys. Fluids **19**, 084104 (2007).

[12] A. Tyliszczak and B. J. Geurts, Controlling spatio-temporal evolution of natural and excited square jets via inlet conditions, Int. J. Heat Fluid Flow **80**, 108488 (2019).

[13] M. B. Alkislar, A. Krothapalli, and G. Butler, The effect of streamwise vortices on the aeroacoustics of a Mach 0.9 jet, J. Fluid Mech. **578**, 139 (2007).

[14] D. Violato and F. Scarano, Three-dimensional evolution of flow structures in transitional circular and chevron jets, Phys. Fluids **23**, 124104 (2011).

[15] K. B. M. Q. Zaman, M. F. Reeder, and M. Samimy, Control of an axisymmetric jet using vortex generators, Phys. Fluids **6**, 778 (1994).

[16] M. F. Reeder and M. Samimy, The evolution of a jet with vortex-generating tabs: Real-time visualization and quantitative measurements, J. Fluid Mech. **311**, 73 (1996).

[17] C. O. Paschereit, I. Wygnanski, and H. E. Fiedler, Experimental investigation of subharmonic resonance in an axisymmetric jet, J. Fluid Mech. **283**, 365 (1995).

[18] J. B. Freund and P. Moin, Jet mixing enhancement by high-amplitude fluidic actuation, AIAA J. **38**, 1863 (2000).

[19] N. Abani and R. D. Reitz, Unsteady turbulent round jets and vortex motion, Phys. Fluids **19**, 125102 (2007).

[20] M. R. Davis, Variable control of jet decay, AIAA J. **20**, 606 (1982).

[21] T. H. New and W. L. Tay, Effects of cross-stream radial injections on a round jet, J. Turbul. **7**, N57 (2006).

[22] J. F. Seidel, C. Pappert, T. H. New, and H. M. Tsai, Effects of multiple radial blowing around a circular jet, in *43rd AIAA Aerospace Sciences Meeting and Exhibit, Reno, Nevada*, 2005.

[23] S. L. Brunton and B. R. Noack, Closed-loop turbulence control: Progress and challenges, Appl. Mech. Rev. **67**, 050801 (2015).

[24] L. N. Cattafesta and M. Sheplak, Actuators for active flow control, Ann. Rev. Fluid Mech. **43**, 247 (2011).

[25] A. K. Perumal and Y. Zhou, Axisymmetric jet manipulation using multiple unsteady minijets, J. Fluid Mech. **848**, 592 (2018).

[26] T. How, D. New, and W. L. Tay, Effects of circumferential microjets on the near-field behaviour of a round jet, in *42nd AIAA Aerospace Sciences Meeting and Exhibit, Reno, Nevada*, 2004.

[27] A. Tyliszczak and B. J. Geurts, Parametric analysis of excited round jets — numerical study, Flow Turb. Combust. **93**, 221 (2014).

[28] G. Broze and F. Hussain, Nonlinear dynamics of forced transitional jets: Periodic and chaotic attractors, J. Fluid Mech. **263**, 93 (1994).

[29] H. Yang and Y. Zhou, Axisymmetric jet manipulated using two unsteady minijets, J. Fluid Mech. **808**, 362 (2016).

[30] T. Shaqarin, Ph.D. thesis, Université de Lille 1, France, 2011.

[31] C. Braud and A. Dyment, Model of an impulsive subsonic jet actuator for flow control applications, Phys. Fluids **24**, 047102 (2012).

[32] P. Wickersham, Ph.D. thesis, Georgia Institute of Technology, Atlanta, 2007.

[33] Y. Zhou, D. Fan, B. Zhang, R. Li, and B. R. Noack, Artificial intelligence control of a turbulent jet, J. Fluid Mech. **897**, A27 (2020).

[34] H. Johari, M. Pachecotougas, and J. Hermanson, Penetration and mixing of fully modulated turbulent jets in crossflow, AIAA J. **37**, 842 (1999).

[35] C. M. Ho and L. S. Huang, Subharmonics and vortex merging in mixing layers, J. Fluid Mech. **119**, 443 (1982).

[36] S. C. Crow and F. H. Champagne, Orderly structure in jet turbulence, J. Fluid Mech. **48**, 547 (1971).

[37] R. T. M'closkey, J. M. King, and L. Cortelezzi, The actively controlled jet in crossflow, J. Fluid Mech. **452**, 325 (2002).

[38] W. C. Reynolds, D. E. Parekh, P. J. D. Juvet, and M. J. D. Lee, Bifurcating and blooming jets, Ann. Rev. Fluid Mech. **35**, 295 (2003).

[39] D. Tamburello and M. Amitay, Manipulation of an axisymmetric jet using a synthetic jet actuator, in *44th AIAA Aerospace Sciences Meeting and Exhibit, Reno, Nevada*, 2006.

[40] J. I. Jiménez-González, P. Brancher, and C. Martínez-Bazán, Modal and non-modal evolution of perturbations for parallel round jets, Phys. Fluids **27**, 044105 (2015).

[41] D. E. Parekh, V. Kibens, A. Glezer, J. M. Wiltse, and D. M. Smith, Innovative jet flow control: Mixing enhancement experiments. AIAA Paper No. 96–0308 (1996).

[42] M. Samimy, J. H. Kim, J. Kastner, I. Adamovich, and Y. Utkin, Active control of high-speed and high-Reynolds-number jets using plasma actuators, J. Fluid Mech. **578**, 305 (2007).

[43] H. Yang, Y. Zhou, R. M. So, and Y. Liu, Turbulent jet manipulation using two unsteady azimuthally separated radial minijets, Proc. R. Soc. London, Ser. A **472**, 20160417 (2016).

[44] A. Perumal, Z. Wu, D. Fan, and Y. Zhou, a hybrid artificial intelligence control of a turbulent jet: Reynolds number effect and scaling, J. Fluid Mech. **942**, A47 (2022).

[45] J. C. Hermanson, A. Wahba, and H. Johari, Duty-cycle effects on penetration of fully modulated, turbulent jets in crossflow, AIAA J. **36**, 1935 (1998).

[46] S. Pothos and E. K. Longmire, Asymmetric forcing of a turbulent rectangular jet with a piezoelectric actuator, Phys. Fluids **13**, 1480 (2001).

[47] D. J. Sailor, D. J. Rohli, and Q. Fu, Effect of variable duty cycle flow pulsations on heat transfer enhancement for an impinging air jet, Int. J. Heat Fluid Flow **20**, 574 (1999).